Materials Horizons

ROYAL SOCIETY OF CHEMISTRY

COMMUNICATION

View Article Online
View Journal | View Issue

Cite this: *Mater. Horiz.*, 2021, **8**, 547

Received 21st September 2020,
Accepted 30th October 2020

DOI: 10.1039/d0mh01521k

rsc.li/materials-horizons

Integrating molecular rigidity and chirality into thermally activated delayed fluorescence emitters for highly efficient sky-blue and orange circularly polarized electroluminescence†

Fan Ni,‡[ab] Chih-Wei Huang,‡[c] Yukun Tang,[c] Zhanxiang Chen,[d] Yaxun Wu,[d] Shengpeng Xia,[d] Xiaosong Cao,[a] Jung-Hsien Hsu,[b] Wei-Kai Lee,[c] Kailu Zheng,[d] Zhongyan Huang,[a] Chung-Chih Wu*[c] and Chuluo Yang*[a]

By integrating high molecular rigidity and stable chirality, two pairs of D*–A type circularly polarized thermally activated delayed fluorescence (CP-TADF) emitters with an almost absolute quasi-equatorial conformer geometry and excellent photoluminescence quantum efficiencies (PLQYs) are developed, achieving state-of-the-art electroluminescence performance among blue and orange circularly polarized organic light-emitting diodes (CP-OLEDs).

New concepts

This work reveals for the first time the importance of a rigid chirality element and fixed molecular configuration in designing thermally activated delayed fluorescence (TADF) emitters with high-performance circularly polarized electroluminescence (CPEL). The concept greatly differs from the previous reports, in which flexible chiral elements are incorporated in TADF emitters to induce circularly polarized luminescence, leading to low photoluminescence quantum efficiencies (PLQYs) and unsatisfactory CPEL performance (*i.e.* the best external quantum efficiency (EQE) is only 12.7% for blue CP-OLEDs and 1.8% for the orange devices). In contrast, the rigid CP-TADF framework in this work provides decent PLQYs (89% for sky-blue and 86% for orange emitters) and an obvious chiral excited singlet state for the emitters, ultimately leading to the most efficient sky-blue and orange CP-OLEDs hitherto reported (EQEs of 20.3% and 23.7%, respectively), while simultaneously featuring intense CPEL signals. The state-of-the-art device performances suggest that the design principle proposed herein is a powerful one for the development of CP-TADF compounds and CP-OLEDs.

Introduction

Circularly polarized organic light-emitting diodes (CP-OLEDs) have gained considerable interest because of their potential application in decreasing light loss arising from the use of a polarizer and a quarter-wave plate in high-contrast OLED displays.[1,2] Despite the rapid enrichment of the chiral luminogenic material library, the development of CP-OLEDs with a satisfactory external quantum efficiency (EQE) and circularly polarized electroluminescence (CPEL) dissymmetry factor (g_{EL}) still remains a formidable challenge.[3–8]

Introduction of the thermally activated delayed fluorescence (TADF) mechanism into circularly polarized luminescent materials turned out to be one successful tactic to boost the efficiency of CP-OLEDs by harnessing both singlet and triplet excitons *via* the thermally activated reverse intersystem crossing (RISC) process.[9] These circularly polarized thermally activated delayed fluorescence (CP-TADF) emitters are typically obtained by installing a chiral element into a twisted D–A-type skeleton.[10] The pioneering research was carried out by Pieters's group and Tang's group by introducing enantiopure 1,1′-bi-2-naphthol (BINOL) into the acceptor, affording green CP-OLEDs with EQEs of up to 9.3% and considerable $|g_{EL}|$ values of up to 9.2×10^{-2}.[10b,d,p] Chen and coworkers designed a chiral 1,2-diaminocyclohexane-based acceptor for CP-TADF emitters and the corresponding green CP-OLEDs achieved EQEs of up to 19.8% and $|g_{EL}|$ values of up to 2.3×10^{-3}.[10c,h] Meanwhile, Zheng's group developed an octahydro-BINOL-based acceptor for green CP-TADF emitters, which revealed high EQEs of up to 32.6% and $|g_{EL}|$ values of 2.3×10^{-3} in devices.[10e,g] In a more recent study, Chen's and Zheng's groups reported axially chiral

[a] *Shenzhen Key Laboratory of Polymer Science and Technology, College of Materials Science and Engineering, Shenzhen University, Shenzhen, 518060, P. R. China. E-mail: clyang@szu.edu.cn*
[b] *Key Laboratory of Optoelectronic Devices and Systems of Ministry of Education and Guangdong Province, College of Optoelectronic Engineering, Shenzhen University, Shenzhen, 518060, P. R. China*
[c] *Department of Electrical Engineering, Graduate Institute of Electronics Engineering and Graduate Institute of Photonics and Optoelectronics, National Taiwan University, Taipei, 10617, Taiwan. E-mail: wucc@ntu.edu.tw*
[d] *Department of Chemistry and Hubei Key Lab on Organic and Polymeric Optoelectronic Materials, Wuhan University, Wuhan, 430072, P. R. China*

† Electronic supplementary information (ESI) available. CCDC 1971785. For ESI and crystallographic data in CIF or other electronic formats, see DOI: 10.1039/d0mh01521k

‡ F. Ni and C. W. Huang contributed equally to this work.

biphenyl unit-based CP-TADF emitters, revealing circularly polarized electroluminescence (CPEL) with EQEs of up to 17.8% and $|g_{EL}|$ values of up to 1.4×10^{-2}.[10l,n,o]

Considerable progress has been made in developing green CP-TADF emitters[10a–e,g,i,n,o] and their corresponding CP-OLEDs have achieved state-of-the-art device performance with EQEs of over 32%.[10e] However, at present, there exist only a few reports on blue[10j–l] and orange[10d,f,h,m] CP-TADF emitters, and the best EQEs of the fabricated CP-OLEDs are 12.7% for blue[10l] and 1.8% for orange,[10f] which are significantly lower than those of their green counterparts. The bottleneck for developing high-performance blue and orange CP-TADF OLEDs is the low PLQYs of the reported CP-TADF emitters (<70% for blue emitters, and <40% for orange emitters), typically caused by the activation of nonradiative transition processes *via* integrating a flexible chirality element into the skeleton. Introducing a chirality element with high rigidity is therefore a prerequisite for constructing excellent blue and orange CP-TADF emitters.

In this work, we designed a point chiral electron donor, namely 12*b*-methyl-5,12*b*-dihydroindeno[1,2,3-*kl*]acridine (MeIAc), by integrating acridine and indene subunits. MeIAc revealed a suitable electron-donating ability, high-lying triplet state energy level and high structural rigidity. MeIAc-derived D*–A type systems, namely 5-(4-(4,6-diphenyl-1,3,5-triazin-2-yl)phenyl)-12*b*-methyl-5,12*b*-dihydr-oindeno[1,2,3-*kl*]acridine (**TRZ-MeIAc**) and 2-(4-(*tert*-butyl)phenyl)-6-(12*b*-methylindeno[1,2,3-*kl*]acridin-5(12b*H*)-yl)-1*H*-benzo[*de*]isoq-uinoline-1,3(2*H*)-dione (**NID-MeIAc**), demonstrated a very rigid molecular architecture, almost absolute quasi-equatorial conformer geometry, obvious TADF behaviour and high PLQYs exceeding 85%. It is worth noting that CP-OLEDs based on the **TRZ-MeIAc** and **NID-MeIAc** enantiomers exhibited highly efficient blue and orange CPEL with excellent performance of maximum EQEs of 20.3% and 23.7%, PEs of 49.6 and 61.3 lm W^{-1} and CEs of 47.8 and 74.5 cd A^{-1}, respectively. To the best of our knowledge, all these parameters represent the highest device performances for all reported blue and orange CP-OLEDs, respectively. Importantly, the high-performance CP-OLEDs also revealed noticeable CPEL signals with $|g_{EL}|$ values of up to 2.4×10^{-3}, indicating efficient chirality transfer of **TRZ-MeIAc** and **NID-MeIAc** in electroluminescence (EL).

Results and discussion

Synthesis and characterization

The newly designed donor of MeIAc was synthesized *via* a three-step route, including Wittig reaction, Pd-catalyzed C–N coupling, and intramolecular cyclization reaction.[11] The target molecules of **TRZ-MeIAc** and **NID-MeIAc** were afforded through Pd-catalyzed C–N coupling reactions between MeIAc and the acceptor 2-(2-bromophenyl)-4,6-diphenyl-1,3,5-triazine or 4-bromo-9-(4-*tert*-butylphenyl)-1,8-naphthalimide (Scheme 1).

The resolution of the two pairs of enantiomers ((*R*/*S*)-**TRZ-MeIAc** and (*R*/*S*)-**NID-MeIAc**) was conducted using a chiral high-performance liquid chromatography column (Fig. S1–S4, ESI†).

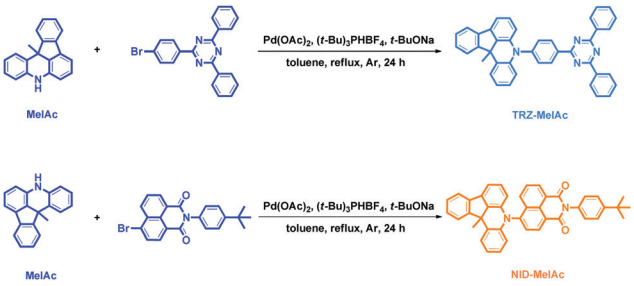

Scheme 1 Synthetic routes of **TRZ-MeIAc** and **NID-MeIAc**.

The enantiomeric excess (e.e.) values of (*R*)-**TRZ-MeIAc**, (*S*)-**TRZ-MeIAc**, (*R*)-**NID-MeIAc** and (*S*)-**NID-MeIAc** enantiomers are 98.2%, 99.6%, 99.2% and 99.6%, respectively. The structure and the absolute configuration of (*R*)-**TRZ-MeIAc** were confirmed using X-ray single crystal analysis (Fig. S5, S6 and Table S1, ESI†). A highly twisted configuration with a nearly orthogonal arrangement was observed between the chiral donor and the phenyl linkage.

The thermal decomposition temperature with 5 wt% loss was found to be 409 °C for **TRZ-MeIAc** and 379 °C for **NID-MeIAc** (Fig. S7 and Table S2, ESI†). The sufficiently high thermal stability makes them suitable candidates for the vacuum deposition process. Cyclic voltammetry (CV) curves of **TRZ-MeIAc** and **NID-MeIAc** in CH_2Cl_2 solution revealed chiral acridine unit-based reversible oxidation behavior (Fig. S9 and Table S2, ESI†). The experimentally obtained highest occupied molecular orbital (HOMO) levels of **TRZ-MeIAc** and **NID-MeIAc** are −5.43 and −5.55 eV, respectively.

Photophysical properties

The basic photophysical properties of the donor unit MeIAc were firstly studied (Fig. S10 and Table S3, ESI†). Attributed to its conjugation-confined architecture, MeIAc revealed a π–π* electronic transition with an absorbance peak centered at 326 nm and ultraviolet emission with a peak around 378 nm in toluene solution. The phosphorescence spectrum of MeIAc in toluene solution at 77 K revealed a typical local-excited feature with multi-peak emission around 439, 469 and 498 nm. The lowest excited triplet (T_1) state energy level determined by the onset of the phosphorescent spectrum is high-lying at 2.91 eV, which can enable the design of CP-TADF emitters with widely tunable emissive colors.

The photophysical properties of **TRZ-MeIAc** and **NID-MeIAc** were then studied in toluene solution (Fig. 1 and Table S4, ESI†). As shown in the absorption spectra, both molecules demonstrated a strong π–π* electronic transition band of the MeIAc subunit and a relatively weak intramolecular charge transfer absorption band (Fig. 1a and b). **TRZ-MeIAc** and **NID-MeIAc** emitted structureless sky-blue and orange light with a distinct enhancement of emission intensity after degassing (inset of Fig. 1c and d). Meanwhile, the transient photoluminescence decay curves in toluene solution of both emitters revealed obvious short-lived (ns-scale) and long-lived (μs-scale) emission in an inert atmosphere, while the long-lived portion was totally quenched after exposure to air (Fig. 1c, d and Table S4, ESI†).

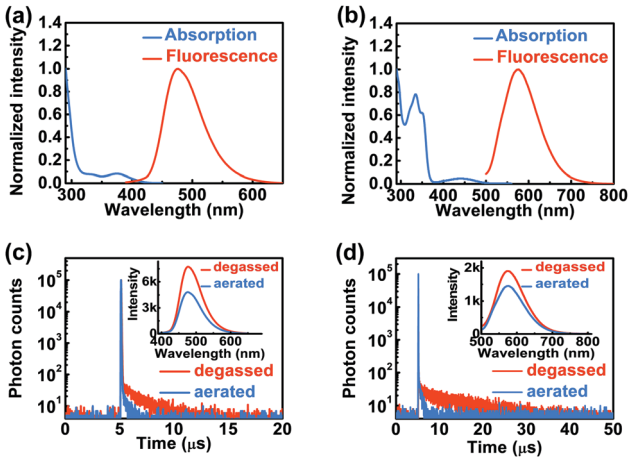

Fig. 1 The absorption and steady-state emission spectra of **TRZ-MeIAc** (a) and **NID-MeIAc** (b) in toluene solution (1.0×10^{-5} M) at room temperature. The transient photoluminescence decay curves of **TRZ-MeIAc** (c) and **NID-MeIAc** (d) in toluene solution (1.0×10^{-5} M) at room temperature before and after degassing. Inset depicts the emission intensity changes of **TRZ-MeIAc** and **NID-MeIAc** in toluene solution at room temperature before and after degassing.

The above results suggested the involvement of an excited triplet state in the emissive process of the two emitters.

To simulate the emissive behaviour in OLEDs, the basic photophysical properties of **TRZ-MeIAc** and **NID-MeIAc** in 9-(3-(9*H*-carbazol-9-yl)phenyl)-9*H*-carbazole-3-carbonitrile (mCPCN) doped films were further measured (Fig. S12, S13, ESI† and Table 1). The 12 wt% **TRZ-MeIAc** doped film emitted structureless blue light with the peak centered at 473 nm (Fig. S12a, ESI†) and the 6 wt% **NID-MeIAc** doped film emitted structureless yellow light with the peak centered at 565 nm (Fig. S13a, ESI†), revealing a charge transfer lowest excited singlet (S_1) state feature. Both of the doped films demonstrated highly efficient emission with PLQYs of 89% for **TRZ-MeIAc** and 86% for **NID-MeIAc**, which are among the highest values for all reported CP-TADF emitters. The ΔE_{ST} values estimated from the fluorescence and phosphorescence spectra of the doped films for **TRZ-MeIAc** and **NID-MeIAc** are 0.19 and 0.22 eV respectively, implying an efficient RISC process. The steady-state emission and transient photoluminescence decay curves of the doped films at different temperatures were further studied (Fig. S12b, c and S13b, c, ESI†). The intensity of the steady-state emission and the ratios of the delayed components increased with increasing temperature, further proving the TADF mechanism.

Based on the basic photophysical data of the doped films at room temperature, the relevant rate constants of the S_1 and T_1 states were then estimated according to a reported method (Table 1 and eqn (S1)–(S12), ESI†).[12] The singlet radiative rates ($k_{r,S}$s) of **TRZ-MeIAc** and **NID-MeIAc** in the doped films were found to be 3.69×10^7 and 1.60×10^7 s^{-1}, respectively, both of which are in the same order of magnitude as that of typical conventional fluorescent emitters (k_r ranging from 10^7 to 10^8 s^{-1}) and much higher than the reported best values of blue (1.18×10^7 s^{-1})[10l] and orange (4.5×10^6 s^{-1})[10f] CP-TADF emitters, respectively. The internal conversion decay rates (k_{IC}^S) of the two emitters were 4.56×10^6 and 2.60×10^6 s^{-1}, respectively. The much slower k_{IC}^Ss than $k_{r,S}$s in the two emitters demonstrate the limited nonradiative decay processes.

Chiroptical properties

The chiroptical properties of the (*R*/*S*)-**TRZ-MeIAc** and (*R*/*S*)-**NID-MeIAc** enantiomers in the ground and excited states were investigated using circular dichroism (CD) and circularly polarized photoluminescence (CPPL) spectra, respectively. The CD spectra in the π–π* transition region (290 to 355 nm for (*R*/*S*)-**TRZ-MeIAc** and 290 to 370 nm for (*R*/*S*)-**NID-MeIAc**) displayed a bisignate Cotton effect (Fig. 2a and d). The absorption peak at 330 nm can be ascribed to the characteristic absorption of the chiral donor (Fig. S10, ESI†). The CD spectra in the charge transfer region (355 to 425 nm for (*R*/*S*)-**TRZ-MeIAc** and 370 to 495 nm for (*R*/*S*)-**NID-MeIAc**) showed a monosignate Cotton effect, indicating that the chirality is successfully transferred from the point chiral donor to the D*–A systems. The CPPL spectra of the two pairs of enantiomers were found to be structureless mirror-symmetric images (Fig. 2b and e), further manifesting the chirality transfer feature in the S_1 states. The luminescence dissymmetry factors (g_{PL}s) are $+5.9 \times 10^{-4}$ for (*R*)-**TRZ-MeIAc**, -5.9×10^{-4} for (*S*)-**TRZ-MeIAc**, $+2.0 \times 10^{-3}$ for (*R*)-**NID-MeIAc** and -2.0×10^{-3} for (*S*)-**NID-MeIAc**, respectively (Fig. 2c and f).

Theoretical simulation

In order to gain more insight into the structure and emissive information of the designed chiral donor and emitters, detailed theoretical calculations based on density functional theory (DFT) and time-dependent DFT were conducted. Serving as a new chiral electron donor, the ground state (S_0) geometrical configurations, contours of the frontier molecular orbitals (FMOs) and energy levels of MeIAc were firstly simulated (Fig. 3, taking (*R*)-MeIAc as an example). By inserting the chiral quaternary carbon, a twisted structural arrangement was obtained in (*R*)-MeIAc (Fig. 3a and b). The acridine unit in

Table 1 Photoluminescence properties of **TRZ-MeIAc** (12 wt%) and **NID-MeIAc** (6 wt%) doped into mCPCN films at room temperature

Compounds	τ_p[a] (ns)	τ_d[a] (μs)	ϕ[b] (%)	ϕ_p[c] (%)	ϕ_d[c] (%)	k_p[d] ($\times 10^7$ s^{-1})	k_d[d] ($\times 10^4$ s^{-1})	$k_{r,S}$[e] ($\times 10^7$ s^{-1})	k_{ISC}[e] ($\times 10^7$ s^{-1})	k_{RISC}[e] ($\times 10^4$ s^{-1})	k_{IC}^S[e] ($\times 10^6$ s^{-1})
TRZ-MeIAc	18.7	82.3	89	69	20	5.35	1.22	3.69	1.20	1.57	4.56
NID-MeIAc	26.3	235.4	86	42	44	3.80	0.42	1.60	1.95	0.87	2.60

[a] The lifetimes of prompt and delayed fluorescence. [b] The total fluorescence PLQY under oxygen-free conditions. [c] The prompt and delayed fluorescence PLQY under oxygen-free conditions. [d] The rate constants of prompt and delayed radiation. [e] The rate constants of singlet radiative decay, intersystem crossing (ISC), reverse intersystem crossing (RISC), and singlet internal conversion (IC) processes.

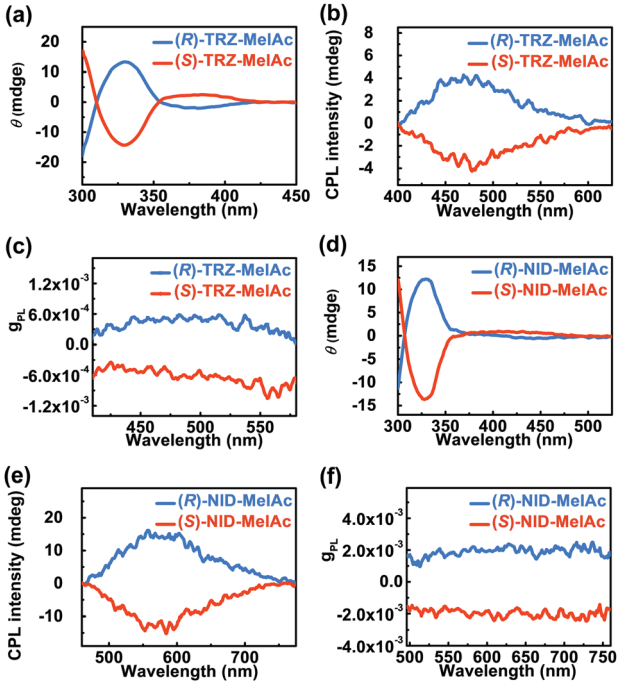

Fig. 2 CD spectra (a), CPPL spectra (b) and g_{PL}s (c) of (*R*/*S*)-**TRZ-MeIAc** in toluene solution (1.0×10^{-4} M). CD spectra (d), CPPL spectra (e) and g_{PL}s (f) of (*R*/*S*)-**NID-MeIAc** in toluene solution (1.0×10^{-4} M).

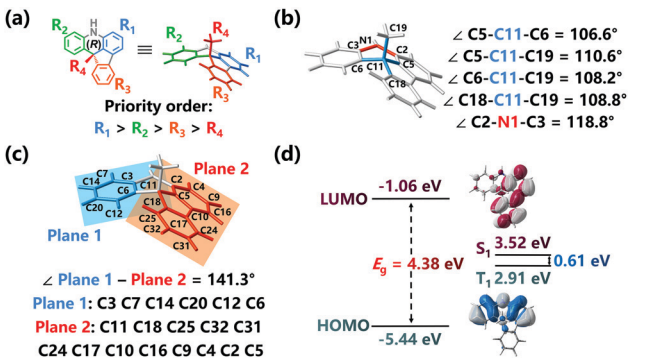

Fig. 3 The optimized ground state structure (a), the geometrical configurations (b) and (c), and the energy levels and contours of the frontier molecular orbitals (d) of (*R*)-MeIAc.

(*R*)-MeIAc was arranged in a "V" shape with a dihedral angle of 141° between the phenyl and fluorenyl units (Fig. 3c). The relatively twisted structural arrangement in (*R*)-MeIAc not only ensured its appropriate electron-donating ability with a HOMO value of −5.44 eV, but also guaranteed a high-lying T_1 state energy level (2.91 eV) with a limited extent of conjugation (Fig. 3d), which matched well with the experimental result and provided the benefit of designing TADF emitters with widely tunable emissive colors.

The theoretical simulation of the S_0 geometry and excited-state energy levels of the two designed molecules was then conducted (Fig. 4, taking (*R*)-**TRZ-MeIAc** and (*R*)-**NID-MeIAc** as examples). Compared with the S_0 state geometry of (*R*)-MeIAc, the optimized S_0 state arrangement of the MeIAc segment in

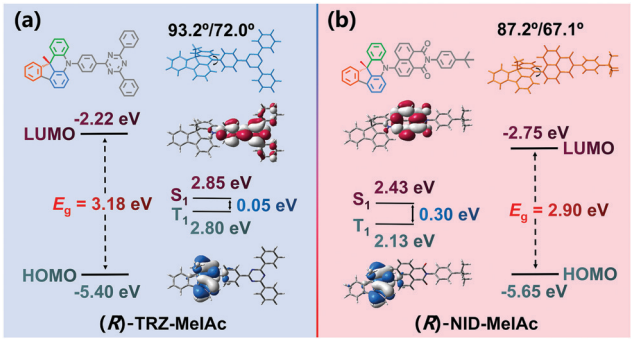

Fig. 4 The geometrical configurations, energy levels and contours of the frontier molecular orbitals of (*R*)-**TRZ-MeIAc** (a) and (*R*)-**NID-MeIAc** (b).

(*R*)-**TRZ-MeIAc** and (*R*)-**NID-MeIAc** showed little deviation, demonstrating the sufficient rigidity of the chiral donor (Fig. S15 and S16, ESI†). Owing to the high steric hindrance, large twisting angles between MeIAc and the acceptor moieties (72.0° and 93.2° for (*R*)-**TRZ-MeIAc** and 67.1° and 87.2° for (*R*)-**NID-MeIAc**, respectively) were obtained. As a result, the HOMOs mainly resided on the acridine component, and the lowest unoccupied molecular orbitals (LUMOs) were localized on the acceptor unit. Such FMO distributions resulted in small ΔE_{ST} values of 0.05 and 0.30 eV for (*R*)-**TRZ-MeIAc** and (*R*)-**NID-MeIAc**, respectively, guaranteeing an efficient RISC process from the T_1 state to the S_1 state to access TADF.

Both of the S_1 states of the two molecules revealed a typical charge transfer (CT) characteristic (96.6% for (*R*)-**TRZ-MeIAc** and 98.4% for (*R*)-**NID-MeIAc**) with the "hole" and "particle" localized at the chiral donor and the achiral acceptor, respectively (Fig. 5). Due to the relatively high T_1 state level of the MeIAc and TRZ units, the T_1 state in **TRZ-MeIAc** was dominant with a charge transfer (^{3}CT) feature (74.1%, Fig. 5a and Fig. S14, ESI†), while owing to the relatively low T_1 state level of the NID unit, the T_1 state of **NID-MeIAc** presented a more locally-excited (^{3}LE) feature (71.2%, Fig. 5b and Fig. S14, ESI†). The spin-orbital coupling (SOC) elements from S_1 to T_1 are 0.401 cm^{-1} for (*R*)-**TRZ-MeIAc** and 0.781 cm^{-1} for (*R*)-**NID-MeIAc**, revealing efficient intersystem crossing (ISC) channels. At the same time, both molecules exhibited strong oscillator strengths (f_s) of singlet transitions (Fig. 5), revealing sufficiently high $S_1 \rightarrow S_0$ radiative rates.

To explain the highly emissive feature of the designed emitters, flexible potential surface scanning of the energy of the S_0 state geometry ((*R*)-**TRZ-MeIAc** and (*R*)-**NID-MeIAc**, for example) was then conducted. Starting from the initial geometries, molecules were optimized (with $\Delta\alpha = \pm 5°$ as a step) to relax the irrational intramolecular interaction force. Due to the asymmetric structure of the donor unit, two local energy maxima exist in (*R*)-**TRZ-MeIAc**, which can be obtained with a rotation angle $\Delta\alpha = 75°$ or 60°. The energy discrepancies between the minimized (quasi-equatorial conformer) and local maximum energy turned out to be 121.5 and 467.9 meV (Fig. 6a). Despite the existence of the minimized local (quasi-axial conformer) and charge transfer state

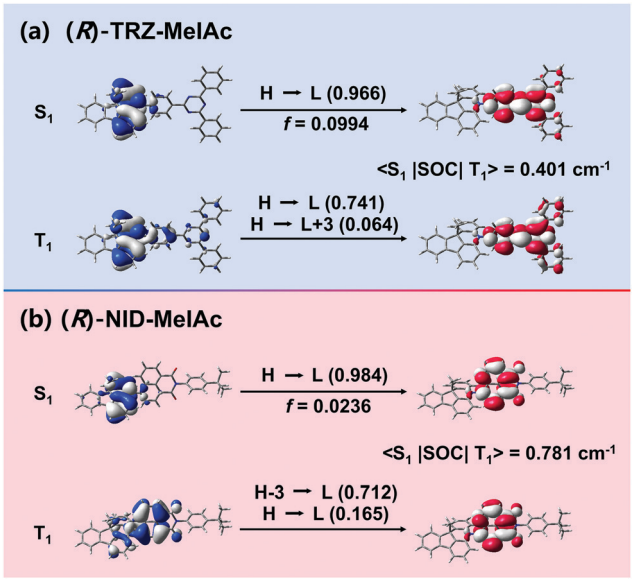

Fig. 5 The "hole" (blue) and "particle" (red) contours, the transition weight of singlet and triplet transitions, the oscillator strength of singlet transitions, and spin–orbit coupling element of (*R*)-**TRZ-MeIAc** (a) and (*R*)-**NID-MeIAc** (b).

(quasi-equatorial conformer), the torsional energy barrier is only 45 meV (much smaller than 126 meV) so the charge transfer S_0 state with a quasi-equatorial conformer is preferred.[13] According to the Boltzmann distribution, the relative ratio of the charge transfer state was determined to be 97.4% (Table S6, ESI†), demonstrating the structural rigidity of MeIAc.[13] Notably, ambient temperature (300 K) with 25 meV energy only allows possible molecular rotation of around $\Delta\alpha = 20^\circ$ in (*R*)-**TRZ-MeIAc**.[14]

The torsional energy barrier between the minimized local (quasi-axial conformer) and charge transfer states (quasi-equatorial conformer) in (*R*)-**NID-MeIAc** is 115 meV (smaller than 126 meV) so the charge transfer S_0 state is predominant (Fig. 6b).[13] The relative ratio of the charge transfer state in (*R*)-**NID-MeIAc** turned out to be larger (more than 99.9%) than that of (*R*)-**TRZ-MeIAc** (97.4%), further demonstrating the rigid structure of MeIAc and the larger steric hindrance leading to a greater extent of charge transfer. In the S_0 state of (*R*)-**NID-MeIAc**, the possible molecular rotation is limited to around $\Delta\alpha = 10^\circ$ at ambient temperature. The potential surface scanning of the energy of the S_1 state geometry was also conducted (Fig. S17, ESI†), revealing a predominant charge transfer feature. The S_1 and S_0 state geometries illustrated little deformation in the two emitters (Fig. 6c and Fig. S15, S16, ESI†) with the root-mean-square deviation (RMSD) of 0.26 Å for (*R*)-**TRZ-MeIAc** and 0.39 Å for (*R*)-**NID-MeIAc**, further indicating the rigid architecture. In light of the above results, it can be realized that the fixed skeleton of the chiral donor and the rigid connection in the two D*–A type molecules provide benefits to enable access to a stable quasi-equatorial conformer for activating TADF and suppressing nonradiative deactivation processes.

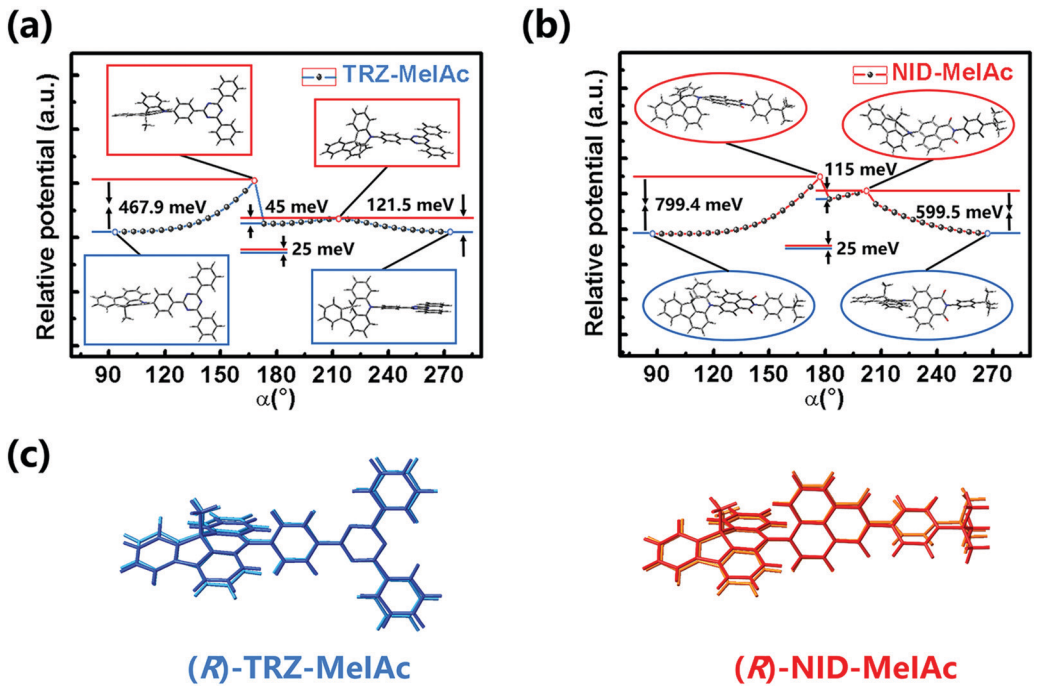

Fig. 6 Flexible potential surface scanning of the energy of the ground state geometry of (*R*)-**TRZ-MeIAc** (a) and (*R*)-**NID-MeIAc** (b) at different twisting angles (α); the maximized local states and the minimized charge transfer states for (*R*)-**TRZ-MeIAc** are labeled with red and blue rectangles respectively; the maximized local states and the minimized charge transfer states of (*R*)-**NID-MeIAc** are labeled with red and blue ellipses, respectively. (c) A comparison of the optimized structures of the S_0 state (light blue) with the S_1 state (blue) of (*R*)-**TRZ-MeIAc** (left) and the S_0 state (orange) with the S_1 state (red) of (*R*)-**NID-MeIAc** (right).

Table 2 The simulated electric ($\vec{\mu}$) and magnetic ($\vec{m}$) transition dipole moment parameters of the **TRZ-MeIAc** and **NID-MeIAc** enantiomers

Emitter	$\lvert\vec{\mu}\rvert^a$ ($\times 10^{-19}$ esu cm)	$\lvert\vec{m}\rvert^b$ ($\times 10^{-21}$ erg per gauss)	R^c ($\times 10^{-40}$ erg esu cm per gauss)	$\cos\theta_{\mu,m}$	$\theta_{\mu,m}{}^d$ (°)	$\frac{\lvert\vec{m}\rvert\cdot\cos\theta_{\mu,m}}{\lvert\vec{\mu}\rvert}L$ ($\times 10^{-3}$)
(*R*)-**TRZ-MeIAc**	4.26	2.04	8.41	0.968	14.5	4.64
(*S*)-**TRZ-MeIAc**	4.26	2.04	−8.41	−0.968	165.5	−4.64
(*R*)-**NID-MeIAc**	2.80	2.17	5.91	0.973	13.3	7.52
(*S*)-**NID-MeIAc**	2.80	2.17	−5.91	−0.973	166.7	−7.52

[a] The simulated electric transition dipole moment value. [b] The simulated magnetic transition dipole moment value. [c] Rotatory strength, $R = \lvert\vec{\mu}\rvert\cdot\lvert\vec{m}\rvert\cdot\cos\theta_{\mu,m}$. [d] The vector angle between the electric and magnetic transition dipole moments.

To obtain more insight into the relationship between the chiral structure and circularly polarized luminescence, theoretical estimation of the electric ($\vec{\mu}$) and magnetic ($\vec{m}$) transition dipole moment was conducted (Table 2).[1a,b,o] The simulated $\lvert\vec{\mu}\rvert$ values of the **TRZ-MeIAc** and **NID-MeIAc** enantiomers are 4.26×10^{-19} and 2.80×10^{-19} esu cm, respectively; the simulated $\lvert\vec{m}\rvert$ values for the two pairs of enantiomers are 2.04×10^{-21} and 2.17×10^{-21} erg per gauss, respectively. When the direction of $\vec{\mu}$ is the same as that of $\vec{m}$ (the charge moves along the right hand spiral path during the transition), positive signals in the CPPL spectrum can be found; otherwise, negative signals would be present. For (*R*)-**TRZ-MeIAc** and (*R*)-**NID-MeIAc**, the vector $\vec{\mu}$ and $\vec{m}$ possessed nearly the same direction (the vector angle $\theta_{\mu,m}$ of 14.5° for (*R*)-**TRZ-MeIAc** and 13.3° for (*R*)-**NID-MeIAc**), in accordance with the positive signals in the CPPL spectra. Meanwhile, (*S*)-**TRZ-MeIAc** and (*S*)-**NID-MeIAc** with nearly opposing directions between the two vectors ($\theta_{\mu,m}$ of 165.5° for (*S*)-**TRZ-MeIAc** and 166.7° for (*S*)-**NID-MeIAc**) demonstrated negative CPPL signals. The simulated $\lvert\vec{\mu}\rvert$ values are much higher than the $\lvert\vec{m}\rvert$ values so the equation for calculating the circularly polarized luminescence dissymmetry factor g can be simplified (eqn (S15), ESI†).[1a,b,k,o]

$$g = 4\mathrm{Re}\left[\frac{\vec{\mu}\cdot\vec{m}}{|\vec{\mu}|^2+|\vec{m}|^2}\right] \approx \mathrm{Re}\left[\frac{|\vec{\mu}|\cdot|\vec{m}|\cdot\cos\theta_{\mu,m}}{|\vec{\mu}|^2}\right] = 4\mathrm{Re}\left[\frac{|\vec{m}|\cdot\cos\theta_{\mu,m}}{|\vec{\mu}|}\right] \quad (1)$$

According to eqn (1), a chiral emitter with a small $\lvert\vec{\mu}\rvert$ value but a large $\lvert\vec{m}\rvert$ value can obtain an ideal $\lvert g\rvert$ value. In the two pairs of CP-TADF emitters, **NID-MeIAc** enantiomers revealed slightly higher $\lvert\vec{m}\rvert$ values but lower $\lvert\vec{\mu}\rvert$ values than those of the **TRZ-MeIAc** enantiomers (Table 2). The higher $\lvert\vec{m}\rvert$ value can be ascribed to the slightly stronger charge-transfer extent (hole → particle, 98.4%) in **NID-MeIAc** than that (hole → particle, 96.6%) in **TRZ-MeIAc** (Fig. 5).[15] The lower $\lvert\vec{\mu}\rvert$ value of **NID-MeIAc** is limited by the relatively weaker oscillator strength (f = 0.0236) compared to that of **TRZ-MeIAc** (f = 0.0994) (Fig. 5 and eqn (S17), ESI†).[1p,16] In addition, with the more parallel/antiparallel direction between the vector $\vec{\mu}$ and $\vec{m}$ ($\lvert\cos\theta_{\mu,m}\rvert$ = 0.968 for **TRZ-MeIAc** enantiomers and $\lvert\cos\theta_{\mu,m}\rvert$ = 0.973 for **NID-MeIAc** enantiomers), the **NID-MeIAc** enantiomers revealed higher $\lvert g\rvert$ values, which is qualitatively consistent with the

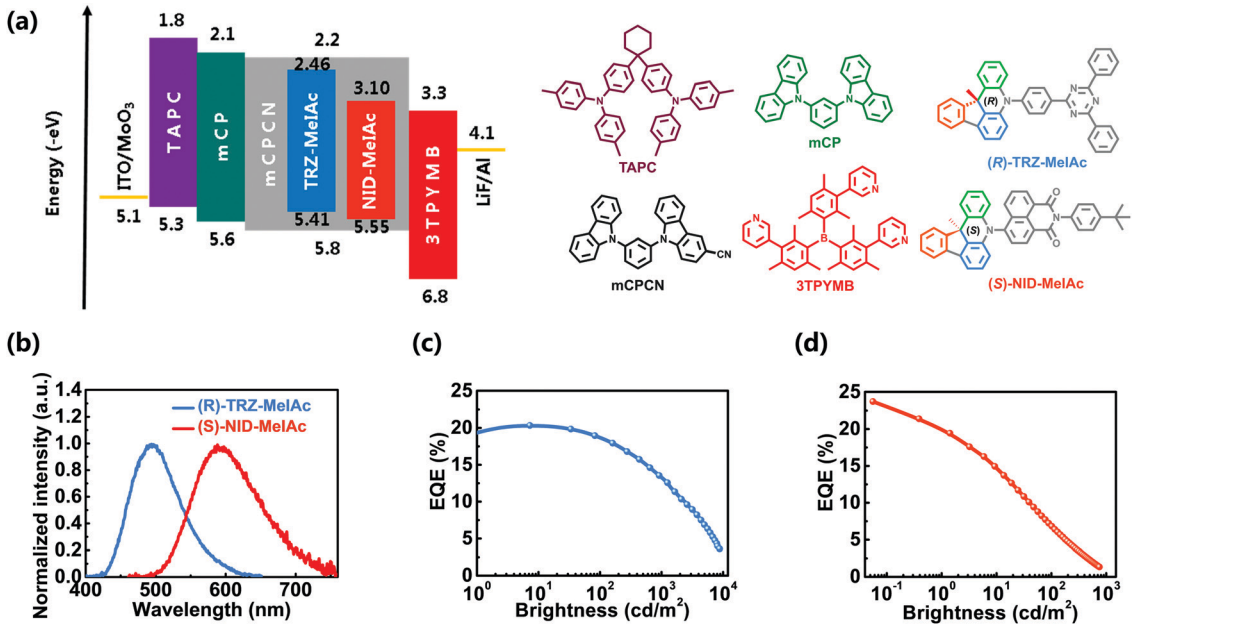

Fig. 7 The device structure, energy level diagram and the molecular structures of the materials employed in the devices (a), electroluminescence spectra (b), and external quantum efficiency characteristics of the optimized devices based on (*R*)-**TRZ-MeIAc** (c) or (*S*)-**NID-MeIAc** (d).

Table 3 A summary of EL data for the optimized devices containing the (*R*/*S*)-**TRZ-MeIAc** and (*R*/*S*)-**NID-MeIAc** enantiomers

Emitter	V_{on}[a] [V]	EL_{peak}[b] [nm]	CE_{max}[c] [cd A^{-1}]	PE_{max}[d] [lm W^{-1}]	EQE_{max}[e] [%]	CIE[f] (*x*, *y*)	g_{EL}[g] [$\times 10^{-4}$]
(*R*)-**TRZ-MeIAc**	2.9	494	47.8	49.6	20.3	(0.18, 0.38)	+6.4
(*S*)-**TRZ-MeIAc**	2.9	494	42.1	44.1	18.7	(0.18, 0.38)	−7.3
(*R*)-**NID-MeIAc**	3.1	591	74.5	42.3	19.0	(0.53, 0.47)	+20
(*S*)-**NID-MeIAc**	3.1	589	68.4	61.3	23.7	(0.53, 0.47)	−24

[a] The turn-on voltage was recorded at a brightness of 1 cd m^{-2}. [b] The peak wavelength of the EL spectrum. [c] The maximum value of current efficiency. [d] The maximum value of power efficiency. [e] The maximum value of external quantum efficiency. [f] The Commission International de l'Eclairage coordinates recorded at the maximum EQE. [g] g_{EL} value of (*R*/*S*)-**TRZ-MeIAc** or (*R*/*S*)-**NID-MeIAc**-based devices at the maximum emission peaks.

experimental results. Based on the above results, designing D*–A type CP-TADF emitters with high molecular rigidity and an enhanced charge transfer feature could simultaneously suppress nonradiative processes and achieve an intense |*g*| value.

CP-OLED performance

Considering the efficient TADF behaviour and obvious CPPL properties, the two pairs of CP-TADF enantiomers were employed as chiral emitters for fabricating OLEDs, with the detailed device structure and related performances displayed in Fig. 7, Table 3 and Fig. S18, S19, Tables S7, S8 (ESI†). The device configuration for **TRZ-MeIAc** (Fig. S18, ESI†) was optimized as follows: ITO (80 nm)/MoO_3 (1 nm)/TAPC (4,4′-(cyclohexane-1,1-diyl)bis(*N*,*N*-di-*p*-tolylaniline)) (45 nm)/mCP (1,3-di(9*H*-carbazol-9-yl)benzene) (10 nm)/mCPCN: (*R*/*S*)-**TRZ-MeIAc** (4 or 8 or 12 wt%) (20 nm)/3TPYMB (tris(2,4,6-trimethyl-3-(pyridin-3-yl)phenyl)-borane) (50 nm)/LiF/Al. ITO and Al acted as the anode and cathode, respectively. MoO_3 and LiF were employed as the hole- and electron-injection layers. TAPC/mCP and 3TPYMB served as the hole- and electron-transporting layers, respectively. With an increase in the doping concentration from 4 wt% to 8 wt%, the device efficiencies were significantly enhanced. For the **NID-MeIAc** enantiomers, the devices adopted a similar architecture except that the thickness of TAPC and 3TPYMB was 70 nm (Fig. S19 and Table S8, ESI†). With an increase in the doping concentration from 1.5 wt% to 3 wt% to 6 wt%, the device efficiencies were gradually boosted.

The two sets of devices based on (*R*/*S*)-**TRZ-MeIAc** and (*R*/*S*)-**NID-MeIAc** displayed sky-blue and orange emission, respectively. The sole emission originated from the emitter in the EL spectrum, indicating efficient energy transfer from the mCPCN host to the CP-TADF dopants. The turn-on voltages for the **TRZ-MeIAc** and **NID-MeIAc** enantiomers were 2.9 V and 3.1 V (Table 3), respectively, demonstrating the well-aligned energy levels of the materials in the device structure.

The OLEDs based on the **TRZ-MeIAc** enantiomers demonstrated obvious mirror-image CPEL activities with opposing g_{EL} values of $+6.4 \times 10^{-4}$ and -7.4×10^{-4} for the *R* and *S* enantiomer-based devices, respectively; while the devices based on (*R*)-**NID-MeIAc** and (*S*)-**NID-MeIAc** displayed g_{EL} values of $+2.0 \times 10^{-3}$ and -2.4×10^{-3}, respectively (Fig. S20 and S21, ESI†). These values are in the same order as the corresponding g_{PL} values. The above results clearly illuminated that the CPEL behavior was inherited from the two pairs of stable and rigid quasi-equatorial CP-TADF enantiomers.

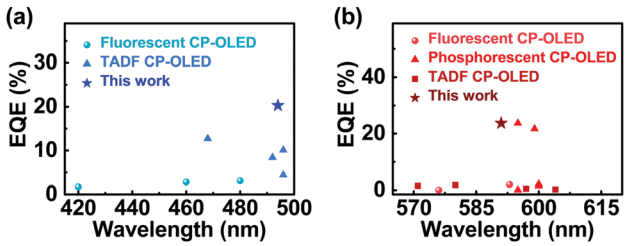

Fig. 8 (a) The EQE values of the reported blue CP-OLEDs (traditional fluorescent (ref. 6*b* and *e*) and TADF (ref. 10*d*, *i* and *l*) CP-OLEDs) and this work. (b) The EQE values of the reported orange to red CP-OLEDs (traditional fluorescent (ref. 6*d* and *e*), phosphorescent (ref. 7*b*, 8*e* and *g*) and TADF (ref. 10*d* and *f*) CP-OLEDs) and this work.

Notably, the rationally designed CP-TADF emitters with high PLQYs provided the corresponding devices with very impressive efficiencies. The optimized (*R*)-**TRZ-MeIAc**-based device showed sky-blue emission with a maximum EQE of 20.3%, a maximum current efficiency (CE) of 47.8 cd A^{-1} and a maximum power efficiency (PE) of 49.6 lm W^{-1}, which are the highest values among all reported blue-emissive CP-OLEDs (Fig. 8a and Table S9, ESI†). It is clear that the efficient harvesting of triplet excitons through the TADF mechanism enabled the superior performance of the **TRZ-MeIAc**-based devices compared to the reported traditional fluorescent CP-OLEDs with blue emission, and the rigid configuration-promoted highly efficient singlet radiative channel in **TRZ-MeIAc** ensured the greater device performance than that of previous blue CP-TADF OLEDs. Meanwhile, the (*S*)-**NID-MeIAc**-based device displayed orange emission, exhibiting a maximum EQE of 23.7%, a maximum CE of 68.4 cd A^{-1} and a maximum PE of 61.3 lm W^{-1}, which represent the state-of-the-art performance among all reported orange CP-OLEDs (Fig. 8b and Table S9, ESI†). The excellent performance compared to that of traditional fluorescence and TADF-based orange CP-OLEDs can be attributed to the efficient exciton harvesting and the highest PLQY.

The EQE is even comparable to the reported best value (23.7%) of iridium complex-based orange CP-OLEDs.[8e] Based on the above results, it can be concluded that designing D*–A type CP-TADF emitters with high rigidity can provide excellent candidates to obtain highly efficient CP-OLEDs.

Conclusions

In conclusion, by integrating acridine and indene subunits, we have ingeniously designed a rigid point chiral TADF donor of

MeIAc and derived two pairs of sky-blue and orange CP-TADF enantiomers, (*R*/*S*)-**TRZ-MeIAc** and (*R*/*S*)-**NID-MeIAc**. These emitters with an almost absolute quasi-equatorial conformer geometry, high molecular rigidity and efficient charge transfer character demonstrated the highest PLQYs and $k_{r,S}$s among the reported blue and orange CP-TADF emitters to date. The corresponding devices displayed state-of-the-art efficiencies in blue and orange CP-OLEDs. Moreover, the stable quaternary carbon stereo-center endowed the corresponding CP-OLEDs with intense $|g_{EL}|$ values of up to 2.4×10^{-3}. This work proves that the rational design of high rigidity D*–A systems can afford efficient charge and chirality transfer and highly emissive CP-TADF emitters for high-performance CP-OLEDs with an intense electroluminescence dissymmetry factor.

Author contributions

F. Ni, C.-W. Huang, X. Cao, C.-C. Wu and C. Yang wrote the manuscript. F. Ni, Y. Wu and S. Xia synthesized the compounds. F. Ni measured the photophysical, thermal and electrochemical properties of the compounds. C.-W. Huang, Y. Tang, J.-H. Hsu, W.-K. Lee and C.-C. Wu fabricated and characterized the devices. F. Ni and C. Yang conceived the original idea for investigation. K. Zheng and Z. Huang performed the X-ray single crystal diffraction analysis. Z. Chen performed the quantum chemical calculations. All authors discussed the progress of research and reviewed the manuscript.

Conflicts of interest

The authors declare no conflict of interest.

Acknowledgements

We gratefully acknowledge the financial support from the National Natural Science Foundation of China (No. 51903161, 91833304 and 21721005), the Shenzhen Science and Technology Program (KQTD20170330110107046), and the China Postdoctoral Science Foundation-funded project (No. 2019M653035). C.-C. Wu acknowledges the support from Ministry of Science and Technology of Taiwan (MOST 107-2221-E-002-160-MY3 and 108-2221-E-002-148-MY3). W.-K. Lee acknowledges the post-doctoral fellowship from Ministry of Education (MOE) and Ministry of Science and Technology (MOST) of Taiwan. The numerical calculations in this paper were performed using the supercomputing system in the Supercomputing Center of Wuhan University. We are particularly grateful to Prof. Y. X. Zheng's group (Nanjing University) for providing the support for CPL measurements.

References

1 (*a*) F. S. Richardson and J. P. Riehl, *Chem. Rev.*, 1977, **77**, 773; (*b*) J. P. Riehl, *Chem. Rev.*, 1986, **86**, 1; (*c*) Y. Zhang and G. B. Schuster, *J. Org. Chem.*, 1995, **60**, 7192; (*d*) N. P. M. Huck, W. F. Jager, B. Lange and B. L. Feringa, *Science*, 1996, **273**, 1686; (*e*) C. Wagenknecht, C. Li, A. Reingruber, X. Bao, A. Goebel, Y. Chen, Q. Zhang, K. Chen and J. Pan, *Nat. Photonics*, 2010, **4**, 549; (*f*) R. Farshchi, M. Ramsteiner, J. Herfort, A. Tahraoui and H. T. Grahn, *Appl. Phys. Lett.*, 2011, **98**, 162508; (*g*) Y. Yang, R. C. Costa, M. J. Fuchter and A. J. Campbell, *Nat. Photonics*, 2013, **7**, 634; (*h*) M. C. Heffern, L. M. Matosziuk and T. J. Meade, *Chem. Rev.*, 2014, **114**, 4496; (*i*) J. Kumar, T. Nakashima and T. Kawai, *J. Phys. Chem. Lett.*, 2015, **6**, 3445; (*j*) G. Longhi, E. Castiglioni, J. Koshoubu, G. Mazzeo and S. Abbate, *Chirality*, 2016, **28**, 696; (*k*) J. R. Brandt, F. Salerno and M. J. Fuchter, *Nat. Rev. Chem.*, 2017, **1**, 0045; (*l*) J. Han, P. Duan, X. Li and M. Liu, *J. Am. Chem. Soc.*, 2017, **139**, 9783; (*m*) K. Takaishi, R. Takehana and T. Ema, *J. Am. Chem. Soc.*, 2018, **140**, 5334; (*n*) Y. Sang, J. Han, T. Zhao, P. Duan and M. Liu, *Adv. Mater.*, 2019, **31**, 1900110; (*o*) N. Berova, P. L. Polavarapu, K. Nakanishi and R. W. Woody, *Comprehensive Chiroptical Spectroscopy, Volume 1: Instrumentation, Methodologies, and Theoretical Simulations*, Wiley, Hoboken, NJ, USA, 1st edn, 2012; (*p*) E. M. Sánchez-Carnerero, A. R. Agarrabeitia, F. Moreno, B. L. Maroto, G. Muller, M. J. Ortiz and S. Moya, *Chem. Eur. J.*, 2015, **21**, 13488.

2 (*a*) M. Grell, M. Oda, K. S. Whitehead, A. Asimakis, D. Neher and D. D. C. Bradley, *Adv. Mater.*, 2001, **13**, 577; (*b*) S. M. Jeong, Y. Ohtsuka, N. Y. Ha, Y. Takanishi, K. Ishikawa, H. Takezoe, S. Nishimura and G. Suzaki, *Appl. Phys. Lett.*, 2007, **90**, 211106; (*c*) R. Singh, K. N. N. Unni, A. Solanki and Deepak, *Opt. Mater.*, 2012, **34**, 716.

3 (*a*) J. Han, S. Guo, H. Lu, S. Liu, Q. Zhao and W. Huang, *Adv. Opt. Mater.*, 2018, **6**, 1800538; (*b*) D. Zhang, M. Li and C. Chen, *Chem. Soc. Rev.*, 2020, **49**, 1331.

4 (*a*) E. Peeters, M. P. T. Christiaans, R. A. J. Janssen, H. F. M. Schoo, H. P. J. M. Dekkers and E. W. Meijer, *J. Am. Chem. Soc.*, 1997, **119**, 9909; (*b*) M. Oda, H. Nothofer, G. Lieser, U. Scherf, S. C. J. Meskers and D. Neher, *Adv. Mater.*, 2000, **12**, 362; (*c*) M. Oda, H. Nothofer, U. Scherf, V. Šunjić, D. Richter, W. Regenstein and D. Neher, *Macromolecules*, 2002, **35**, 6792; (*d*) Y. Geng, A. Trajkovska, S. W. Culligan, J. J. Ou, H. M. P. Chen, D. Katsis and S. H. Chen, *J. Am. Chem. Soc.*, 2003, **125**, 14032; (*e*) D. D. Nuzzo, C. Kulkarni, B. Zhao, E. Smolinsky, F. Tassinari, S. C. J. Meskers, R. Naaman, E. W. Meijer and R. H. Friend, *ACS Nano*, 2017, **11**, 12713; (*f*) L. Yang, Y. Zhang, X. Zhang, N. Li, Y. Quan and Y. Cheng, *Chem. Commun.*, 2018, **54**, 9663.

5 (*a*) Y. Yang, R. C. Costa, D.-M. Smilgies, A. J. Campbell and M. J. Fuchter, *Adv. Mater.*, 2013, **25**, 2624; (*b*) D. Lee, J. Song, Y. Lee, C. Yu and J. Kim, *Adv. Mater.*, 2017, **29**, 1700907; (*c*) J. Jung, D. Lee, J. Kim and C. Yu, *J. Mater. Chem. C*, 2018, **6**, 726.

6 (*a*) Y. Zhang, X. Zhang, H. Zhang, Y. Xiao, Y. Quan, S. Ye and Y. Cheng, *J. Phys. Chem. C*, 2019, **123**, 24746; (*b*) X. Zhang, Y. Zhang, Y. Li, Y. Quan, Y. Cheng and Y. Li, *Chem. Commun.*, 2019, **55**, 9845; (*c*) X. Zhang, Y. Zhang, H. Zhang, Y. Quan, Y. Li, Y. Cheng and S. Ye, *Org. Lett.*, 2019, **21**, 439; (*d*) Y. Chen, X. Li, N. Li, Y. Quan, Y. Cheng and Y. Tang, *Mater. Chem. Front.*, 2019, **3**, 867; (*e*) X. Luo,

H. Han, Z. Yan, Z. Wu, J. Su, J. Zou, Z. Zhu, Y. Zheng and J. Zuo, *ACS Appl. Mater. Interfaces*, 2020, **12**, 23172.

7 (*a*) F. Zinna, U. Giovanella and L. D. Bari, *Adv. Mater.*, 2015, **27**, 1791; (*b*) F. Zinna, M. Pasini, F. Galeotti, C. Botta, L. D. Bari and U. Giovanella, *Adv. Funct. Mater.*, 2017, **27**, 1603719.

8 (*a*) T. Li, Y. Jing, X. Liu, Y. Zhao, L. Shi, Z. Tang, Y. Zheng and J. Zuo, *Sci. Rep.*, 2015, **5**, 14912; (*b*) J. R. Brandt, X. Wang, Y. Yang, A. J. Campbell and M. J. Fuchter, *J. Am. Chem. Soc.*, 2016, **138**, 9743; (*c*) J. Han, S. Guo, J. Wang, L. Wei, Y. Zhuang, S. Liu, Q. Zhao, X. Zhang and W. Huang, *Adv. Opt. Mater.*, 2017, **5**, 1700359; (*d*) Z. Yan, X. Luo, W. Liu, Z. Wu, X. Liang, K. Liao, Y. Wang, Y. Zheng, L. Zhou, J. Zuo, Y. Pan and H. Zhang, *Chem. – Eur. J.*, 2019, **25**, 5672; (*e*) Z. Yan, K. Liao, H. Han, J. Su, Y. Zheng and J. Zuo, *Chem. Commun.*, 2019, **55**, 8215; (*f*) G. Fu, Y. He, W. Li, B. Wang, X. Lü, H. He and W.-Y. Wong, *J. Mater. Chem. C*, 2019, **7**, 13743; (*g*) Z. Jiang, J. Wang, T. Gao, J. Ma, Z. Liu and R. Chen, *ACS Appl. Mater. Interfaces*, 2020, **12**, 9520.

9 (*a*) H. Uoyama, K. Goushi, K. Shizu, H. Nomura and C. Adachi, *Nature*, 2012, **492**, 234; (*b*) Y. Tao, K. Yuan, T. Chen, P. Xu, H. Li, R. Chen, C. Zheng, L. Zhang and W. Huang, *Adv. Mater.*, 2014, **26**, 7931; (*c*) M. Y. Wong and E. Zysman-Colman, *Adv. Mater.*, 2017, **29**, 1605444; (*d*) Z. Yang, Z. Mao, Z. Xie, Y. Zhang, S. Liu, J. Zhao, J. Xu, Z. Chi and M. P. Aldred, *Chem. Soc. Rev.*, 2017, **46**, 915; (*e*) Y. Im, M. Kim, Y. J. Cho, J. A. Seo, K. S. Yook and J. Y. Lee, *Chem. Mater.*, 2017, **29**, 1946; (*f*) J. Guo, Z. Zhao and B. Z. Tang, *Adv. Opt. Mater.*, 2018, **6**, 1800264; (*g*) Y. Zou, S. Gong, G. Xie and C. Yang, *Adv. Opt. Mater.*, 2018, **6**, 1800568; (*h*) F. Ni, N. Li, L. Zhan and C. Yang, *Adv. Opt. Mater.*, 2020, **8**, 1902187.

10 (*a*) T. Imagawa, S. Hirata, K. Totani, T. Watanabea and M. Vacha, *Chem. Commun.*, 2015, **51**, 13268; (*b*) S. Feuillastre, M. Pauton, L. Gao, A. Desmarchelier, A. J. Riives, D. Prim, D. Tondelier, B. Geffroy, G. Muller, G. Clavier and G. Pieters, *J. Am. Chem. Soc.*, 2016, **138**, 3990; (*c*) M. Li, S. Li, D. Zhang, M. Cai, L. Duan, M. Fung and C. Chen, *Angew. Chem., Int. Ed.*, 2018, **57**, 2889; (*d*) F. Song, Z. Xu, Q. Zhang, Z. Zhao, H. Zhang, W. Zhao, Z. Qiu, C. Qi, H. Zhang, H. H. Y. Sung, I. D. Williams, J. W. Y. Lam, Z. Zhao, A. Qin, D. Ma and B. Z. Tang, *Adv. Funct. Mater.*, 2018, **28**, 1800051; (*e*) Z. Wu, H. Han, Z. Yan, X. Luo, Y. Wang, Y. Zheng, J. Zuo and Y. Pan, *Adv. Mater.*, 2019, **31**, 1900524; (*f*) Y. Wang, Y. Zhang, W. Hu, Y. Quan, Y. Li and Y. Cheng, *ACS Appl. Mater. Interfaces*, 2019, **11**, 26165; (*g*) Z. Wu, Z. Yan, X. Luo, L. Yuan, W. Liang, Y. Wang, Y. Zheng, J. Zuo and Y. Pan, *J. Mater. Chem. C*, 2019, **7**, 7045; (*h*) Y. Wang, H. Lu, C. Chen, M. Li and C. Chen, *Org. Electron.*, 2019, **70**, 71; (*i*) S. Sun, J. Wang, L. Chen, R. Chen, J. Jin, C. Chen, S. Chen, G. Xie, C. Zheng and W. Huang, *J. Mater. Chem. C*, 2019, **7**, 14511; (*j*) N. Sharma, E. Spuling, C. M. Mattern, W. Li, O. Fuhr, Y. Tsuchiya, C. Adachi, S. Bräse, I. D. W. Samuel and E. Zysman-Colman, *Chem. Sci.*, 2019, **10**, 6689; (*k*) Y. Hu, F. Song, Z. Xu, Y. Tu, H. Zhang, Q. Cheng, J. W. Y. Lam, D. Ma and B. Z. Tang, *ACS Appl. Polym. Mater.*, 2019, **1**, 221; (*l*) M. Li, Y. Wang, D. Zhang, L. Duan and C. Chen, *Angew. Chem., Int. Ed.*, 2020, **59**, 3500; (*m*) F. Hao, Y. Shi, K. Wang, S. Xiong, X. Fan, L. Wu, C. Zheng, Y. Li, X. Ou and X. Zhang, *Dyes Pigm.*, 2020, **178**, 108336; (*n*) Z. Tu, Z. Yan, X. Liang, L. Chen, Z. Wu, Y. Wang, Y. Zheng, J. Zuo and Y. Pan, *Adv. Sci.*, 2020, **7**, 2000804; (*o*) Y. Wang, M. Li, W. Zhao, Y. Shen, H. Lu and C. Chen, *Chem. Commun.*, 2020, **56**, 9380; (*p*) L. Frédéric, A. Desmarchelier, R. Plais, L. Lavnevich, G. Muller, C. Villafuerte, G. Clavier, E. Quesnel, B. Racine, S. Meunier-Della-Gatta, J.-P. Dognon, P. Thuéry, J. Crassous, L. Favereau and G. Pieters, *Adv. Funct. Mater.*, 2020, **30**, 2004838; (*q*) S. Yang, Y. Wang, C. Peng, Z. Wu, S. Yuan, Y. Yu, H. Li, T. Wang, H. Li, Y. Zheng, Z. Jiang and L. Liao, *J. Am. Chem. Soc.*, 2020, **142**, 17756.

11 Z. Gu, C. Liu, S. Wang and S. Ji, *Org. Lett.*, 2016, **18**, 2379.

12 K. C. Pan, S. W. Li, Y. Y. Ho, Y. J. Shiu, W. L. Tsai, M. Jiao, W. K. Lee, C. C. Wu, C. L. Chung and T. Chatterjee, *Adv. Funct. Mater.*, 2016, **26**, 7560.

13 (*a*) Y. Olivier, M. Moral, L. Mucciolicd and J.-C. Sancho-García, *J. Mater. Chem. C*, 2017, **5**, 5718; (*b*) K. Wang, C. Zheng, W. Liu, K. Liang, Y. Shi, S. Tao, C. Lee, X. Ou and X. Zhang, *Adv. Mater.*, 2017, **29**, 1701476; (*c*) W. Li, X. Cai, B. Li, L. Gan, Y. He, K. Liu, D. Chen, Y. Wu and S. Su, *Angew. Chem., Int. Ed.*, 2019, **58**, 582.

14 (*a*) W. Li, D. Liu, F. Shen, D. Ma, Z. Wang, T. Feng, Y. Xu, B. Yang and Y. Ma, *Adv. Funct. Mater.*, 2012, **22**, 2797; (*b*) L. Yao, Y. Pan, X. Tang, Q. Bai, F. Shen, F. Li, P. Lu, B. Yang and Y. Ma, *J. Phys. Chem. C*, 2015, **119**, 17800; (*c*) X. Cai, X. Li, G. Xie, Z. He, K. Gao, K. Liu, D. Chen, Y. Cao and S. Su, *Chem. Sci.*, 2016, **7**, 4264.

15 (*a*) J. Yeom, U. S. Santos, M. Chekini, M. Cha, A. F. Moura and N. A. Kotov, *Science*, 2018, **359**, 309; (*b*) J. Han, D. Yang, X. Jin, Y. Jiang, M. Liu and P. Duan, *Angew. Chem., Int. Ed.*, 2019, **58**, 7013.

16 (*a*) R. C. Hilborn, *Am. J. Phys.*, 1982, **50**, 982; (*b*) M. Uejima, T. Sato, D. Yokoyama, K. Tanaka and J.-W. Park, *Phys. Chem. Chem. Phys.*, 2014, **16**, 14244; (*c*) X. Mu, X. Chen, J. Wang and M. Sun, *J. Phys. Chem. A*, 2019, **123**, 8071.